



20 **ABSTRACT**

21  
22 *Rationale:* Medical radioisotopes produce Cerenkov luminescence (CL) from charged subatomic  
23 particles ( $\beta^{\pm}$ ) travelling faster than light in dielectric media (e.g. tissue). CL is a blue-weighted  
24 and continuous emission, decreasing proportional to wavelength. CL imaging (CLI) provides an  
25 economical PET alternative with the advantage of being able to image  $\beta^-$  and  $\alpha$  emitters. Like any  
26 optical modality CLI is limited by the optical properties of tissue (scattering, absorption and  
27 ambient photon removal). Shortwave infrared (SWIR, 900 – 1700 nm) CL has been detected from  
28 MeV linear accelerators but not yet from KeV medical radioisotopes. *Methods:* Indium gallium  
29 arsenide (InGaAs) sensors and SWIR lenses were mounted onto an ambient light excluding  
30 preclinical enclosure. An exposure and processing pipeline was developed with SWIR CLI then  
31 performed across 6 radioisotopes at *in vitro* and *in vivo* conditions. *Results:* SWIR CL was  
32 detected from the clinical radioisotopes:  $^{90}\text{Y}$ ,  $^{68}\text{Ga}$ ,  $^{18}\text{F}$ ,  $^{89}\text{Zr}$ ,  $^{131}\text{I}$  and  $^{32}\text{P}$  (biomedical research).  
33 SWIR CLI's advantage over visible (VIS, 400 – 900 nm) CLI is shown via increased light  
34 penetration and decreased scattering at depth. The radioisotope SWIR spectrum, sensitivity limits  
35 (8.51 kbq/ $\mu\text{L}$  of  $^{68}\text{Ga}$ ) and preclinical feasibility with *ex vivo* and *in vivo* examples are reported.  
36 *Conclusion:* This work shows that radioisotope SWIR CLI can be performed with unmodified  
37 commercially available components. SWIR CLI has significant advantages over VIS CLI with  
38 preserved VIS CLI features such as radioisotope radiance levels and dose response linearity.  
39 Further improvements in SWIR optics and technology are required to enable widespread  
40 adoption.

41  
42 **Keywords:** SWIR, Cerenkov, luminescence, radioisotopes, preclinical

43

## 44 INTRODUCTION

45  
46 Subatomic relativistic particles generate CL in dielectric media.(1) The particle polarizes  
47 surrounding molecules, which generate luminescence upon relaxation (2) with CL being UV  
48 weighted. CL production decreases exponentially with increasing wavelength ( $1/\lambda^2$ ). (3) CL's  
49 intensity – but not the spectrum profile - is correlated to the energy of the emitted particle and has  
50 been utilized in astrophysics, nuclear physics, and recently in biomedical imaging.(4,5) CL  
51 imaging (CLI) is a cost- and time-effective positron emission tomography (PET) alternative for  
52 surface-weighted imaging, e.g. for triaging patients into those who do not need a PET and those  
53 who do.(2,6,7) CLI has focused on CL detection from clinical beta ( $\beta^{\pm}$ ) emitting radioisotopes and  
54 linear accelerators (LINAC).(4,8,9) Preclinical discoveries and development of novel targeted  
55 radiotracers, dosimetry and radiotherapy-based treatments have been aided by CLI.(10,11)  
56 Clinical CLI has also found applications in image guided surgery for margin detection, determining  
57 the clinical uptake of radiotracers and real time dosimetry readings.(7, 12-15)

58  
59 Single photon sensitive devices responsive to the CL spectrum are readily available, providing  
60 low dark and read noise optical devices.(2) However, visible wavelengths (VIS, 400 – 900 nm)  
61 suffer significant drawbacks in pre/clinical settings. Endogenous chromophores limit the  
62 achievable VIS CL penetration depths with scattering further reducing resolution, contrast and  
63 sensitivity of VIS CLI at depth.(16,17) Optical imaging has shifted to longer wavelengths where  
64 light absorption and scattering are reduced.(18) Near infrared (NIR) imaging (>650 nm) reduces  
65 absorption by ~2 orders of magnitude.(16,19) Studies employed dyes and nanoparticles for red  
66 shifted conversion of CL.(20-22) SWIR imaging has shown tissue absorption, scattering and  
67 autofluorescence are of negligible levels.(23) SWIR's advantages for resolution and contrast have  
68 been shown via clinically approved indocyanine green.(24) Förster resonance energy transfer  
69 based SWIR CL has been achieved via X-ray excited nanoprobe and LINAC excited emission  
70 of quantum dots.(20,25-27) LINAC SWIR CLI has been performed without secondary emitters  
71 showing improvements over VIS-NIR CLI.(28) Radioisotopes produce an order of magnitude less  
72 CL than LINACs and are therefore more demanding to image (LINAC: 6 to 24 MeV,  $^{68}\text{Ga}$ : 0.836  
73 MeV).(29-32) Radioisotope CLI requires complete exclusion of ambient light, efficient optical  
74 imaging systems and cannot be pulse synchronized in its acquisition like LINAC CLI.(30,33) The  
75 already low CL radiance of radioisotopes is even further reduced at SWIR wavelengths,  
76 magnifying the difficulty of SWIR CL detection.(3) Nevertheless, SWIR CLI from radioisotopes  
77 was achieved via unmodified and commercially available imaging components and revealed  
78 defined advantages over VIS CLI.

## 80 MATERIALS AND METHODS

### 82 Radioisotope SWIR Setup

83  
84 SWIR CLI was achieved via commercially available InGaAs focal plane arrays (NIRvana 640  
85 TE, Princeton Teledyne, NJ, USA or ZephIR 1.7x, Photon etc Inc., Montreal, Canada) and SWIR  
86 lens set to  $f/1.4$  (SWIR-16, Navitar, NY, USA or 8mm SWIR lens, #83-815, Edmund Optics, NJ,  
87 USA) mounted on an enclosure, Figure 1. Figures 1, B – E acquired without optical filters,  
88 (NIRvana 640 TE, 900 – 1700 nm).(34) All other figures employed a 650nm or 900 nm O.D. 4.0  
89 long pass (LP) filter (Edmund Optics #84-759 and #84-764, NJ, USA). Acquisition (90, 10s frames  
90 (15mins)) was controlled via respective acquisition software. Dark noise was recorded and  
91 subtracted for each sensor. White light (WL) images, acquired with room lights on, enclosure door  
92 open, room lights with SWIR spectral emission (Pentron 3000K, Osram Sylvania, MA, USA).(35)  
93 Radioisotopes were imaged in containers within a lead pig. Black posterboard (TB5, Thorlabs,  
94 NJ, USA) was used to absorb CL and allow  $\gamma$  particles to pass.

95  
96  
97  
98  
99  
100  
101  
102  
103  
104  
105  
106  
107  
108  
109  
110  
111  
112  
113  
114  
115  
116  
117  
118  
119  
120  
121  
122  
123  
124  
125  
126  
127  
128  
129  
130  
131  
132  
133  
134  
135  
136  
137  
138  
139  
140  
141  
142  
143  
144  
145

## Determining the Radioisotope SWIR CLI Temporal Resolution and Emission Spectrum

SWIR CL temporal resolution and spectrum were determined using 370 Mbq of  $^{32}\text{P}$  in 1 ml of water ( $\beta^-$ : average 0.695MeV,  $t_{1/2}$  14.3 days, NEX060005MC, Perkin Elmer, MA, USA). 90 frame acquisitions at respective exposure times were performed, Figure 1D and Supplemental Figure 1. The limit of detection was defined when SWIR CL was not determinable from the noise. LP filters (1000-1500 nm in 100 nm steps (FELH1000:100:1500, SM1L03 and SM1A57, Thorlabs, NJ, USA) elucidated the radioisotope spectrum.

## Image Processing and Statistical Analysis

Fiji (ImageJ 2.0, (36)) was used for image processing, Supplementary Figure 2. Darknoise was subtracted from the data with binning (8x8, to improve sensitivity), median filtering (outlier,  $\gamma$  strike removal), FFT bandpass transformations (artifact removal) and background subtraction applied.(37) Images were resized for WL overlays. Statistical analysis, graphing: performed in GraphPad Prism9 (GraphPad Software LLC, CA, USA). Statistical analyses and replicate information are shown in all cases. Radiance was calculated via gray values corrected for isotope concentration (kbq/ $\mu\text{L}$ ) and field of view (FOV,  $\text{cm}^2$ ). Full width half maximum measurements were carried in MATLAB (2020b, Mathworks Inc., USA).

## Silica Nanoparticle Radiolabeling and Injection

Silica nanoparticles (SiNPs) were labeled with  $^{68}\text{Ga}$  or  $^{90}\text{Y}$  as described.(38) Silica nanoparticles (SiNPs) were incubated with free isotope at a pH of 8.8 for 60 mins, on a thermomixer at 70°C and 500 rpm. Radiolabeled SiNPs were resuspended in 30  $\mu\text{l}$  of saline for footpad injection.

## Preclinical SWIR CLI

All experiments were carried out in accordance with Institutional Animal Care and Use Committee (IACUC) guidelines at MSKCC and the NIH Guide for the Care and Use of Laboratory Animals. 3% isoflurane in 100%  $\text{O}_2$  v/v followed by 1-2% isoflurane in 100%  $\text{O}_2$  v/v for maintenance for anesthesia, euthanasia was performed using  $\text{CO}_2$  in accordance with approved protocols. All mice ( $n = 13$  in total, FoxN1<sup>NU</sup>, Stock #069, Envigo, USA) were suitably housed with food and water *ad libitum*.  $1 \times 10^6$  4T1 cells (ATCC, CRL-2539) suspended in 30  $\mu\text{l}$  of Matrigel (Corning, #354234) into the fourth mammary pad generated xenograft mice ( $n = 4$ ). Supplementary Figure 3, 3 euthanised xenografted mice were injected (blinded) with up to 166.5 Mbq of  $^{18}\text{F}$ -FDG with one mouse acting as a negative control. 1 euthanized mouse was injected into the footpad with  $^{68}\text{Ga}$  labeled SiNPs. 4 mice were injected with  $^{90}\text{Y}$  labeled SiNPs with an additional one mouse acting as a negative control for *in vivo* experiments.

## RESULTS

### Confirmation of SWIR CL Detection from Radioisotopes

The SWIR CLI radioisotope setup is shown (Figure 1A) detecting  $^{68}\text{Ga}$  suspended in 0.1M HCl.(39,40). Figure 1B top right, shows the processed SWIR CL image overlaid onto the WL image. This demonstrates that SWIR signal is coming from  $^{68}\text{Ga}$  and that the processing steps sufficiently removed strikes whilst retaining CL signals. CL detection is further confirmed by a lack of signal when cardboard was placed over the sample, Figure 1B, blocking light but not the highly

146 energetic photons from  $^{68}\text{Ga}$ 's decay (e.g. 511 & 1077 keV). The  $^{68}\text{Ga}$  source was further moved  
147 and detected around the FOV, decaying in the process, visible via a decreasing SWIR signal,  
148 following the decay half life of the isotope. Manual regions of interest (ROI) were measured to  
149 determine the signal intensity (gray values) of the sensor for each position and timepoint. SWIR  
150 CLI showed quantitative linearity to  $^{68}\text{Ga}$  levels like VIS CLI.(4) We then successfully detected  
151 four additional radioisotopes under comparative conditions:  $^{32}\text{P}$ ,  $^{18}\text{F}$ ,  $^{89}\text{Zr}$  and  $^{131}\text{I}$ , Figure 1 and  
152 Supplementary Figure 4. The SWIR radiance of each was calculated as before (Figure 1) with  
153 values corrected for concentration (kbq/ $\mu\text{L}$ ) and spatial FOV ( $\text{cm}^2$ ). SWIR CLI readily  
154 differentiated the tested radioisotopes in line with VIS CLI, as shown by the p values in Figure  
155 2B.(41,42) Theoretically  $^{68}\text{Ga}$  has a higher radiance than  $^{32}\text{P}$  however, the increased sensor strikes  
156 from 511 & 1077 keV photons by  $^{68}\text{Ga}$  prevent SWIR CLI from confirming this as the setup did  
157 not incorporate lead shielding.(42)

158

### 159 **SWIR CLI Radioisotope Temporal Detection Limit and Emission Spectrum**

160

161 System characterization was performed using  $^{32}\text{P}$  ( $\beta^-$ ) with concentrations used to facilitate  
162 SWIR CLI at a temporal resolution of 0.25s, Figure 1 and Supplemental Figure 1.  $^{32}\text{P}$ 's radiance  
163 and half-life enabled determination of the radioisotope SWIR CL emission spectrum.(42) No filter  
164 (>920nm, spectral response of the sensor) and LP filtered acquisitions (1000-1500 nm, 100 nm  
165 steps) were carried out. This sensor has a non-thinned indium phosphide (InP) substrate bandgap  
166 (1.35 eV) preventing detection of light <920 nm whilst the bandgap of InGaAs (0.75 eV) results in  
167 a shortpass cutoff at 1700nm.(43-45) The radioisotope SWIR CL spectrum is shown in Figure 1E  
168 with intensity exponentially decreasing (one phase exponential decay,  $R^2 = 0.9812$ ), as expected  
169 and reported for VIS CLI and LINAC SWIR CLI.(2,28) Detection above 1400nm is challenging  
170 due to system noise, lens inefficiency and water absorption, see Figure 1E and F and  
171 Supplemental Figures 1 and 7.(19,46)

172

### 173 **Reduced Scattering via SWIR CLI over VIS CLI**

174

175 55.5 Mbq of  $^{90}\text{Y}$  in an Eppendorf ( $\beta^-$  emitter, Avg 0.94 MeV,  $t_{1/2}$  64h in 200  $\mu\text{l}$  of saline) was  
176 imaged on both the SWIR and IVIS<sup>®</sup> (VIS CLI, 400 – 900 nm) imaging systems to assess the  
177 advantages of SWIR CLI.  $^{90}\text{Y}$  is clinically administered from 0.500 to 5.291 Gbq to treat primary  
178 liver cancer (HCC) and metastases in the liver.(47,48) Scattering medium (raw chicken breast, 0,  
179 10 and 15 mm) was placed over the source prior to CLI being performed. Respective exposure  
180 times without scattering medium (VIS CLI: 10s, SWIR CLI: 900s) were maintained at all depths.  
181 SWIR CLI shows an improvement in resolution compared to VIS CLI when imaging through  
182 scattering tissue (Figure 2). In SWIR CLI the Eppendorf shape is consistent up to 15 mm of tissue  
183 whilst it is distorted and enlarged over five times from scatter in VIS CLI. SWIR CLI provides  
184 greater resolution at depth over VIS CLI for radioisotope location. This accuracy is demonstrated  
185 by the full width half maximum (FWHM) measurements of 6.38, 13.05 and 33.64 mm for VIS CLI  
186 and 6.24, 6.40 and 7.04 mm for SWIR CLI at 0, 10 & 15 mm of tissue, respectively (Figure 2).

187

### 188 **SWIR CLI Radioisotope Sensitivity Limits *in vitro* and *ex vivo***

189

190 Commercial SWIR sensors are insensitive to light <920nm without InP cap thinning. In  
191 systems with InP thinning the sensor has a largely increased range, but is rather insensitive  
192 compared to EMCCDs. One such SWIR sensor (Zephir 1.7x, Photon Etc., Canada) was used  
193 with significantly reduced QE in the VIS range (~25% at 600 nm). The sensor enabled a  
194 comparison of the spatial localization of radioisotope VIS-SWIR (400 – 1700 nm), NIR-SWIR (650  
195 – 1700 nm) and SWIR (900 – 1700 nm) CLI.  $^{68}\text{Ga}$  conjugated SiNPs (in 30  $\mu\text{l}$  of saline) opposite  
196 a non-radiolabeled SiNP control were imaged at VIS-SWIR, NIR-SWIR, and at SWIR for

197 numerous half-lives via appropriate LP filters. The detected CL signals are localized to the  
198 radiolabelled SiNPs throughout the spectrums (Supplemental Figure 5A-D). The detection limit of  
199 radioisotope SWIR CLI is at 259 kbq (8.51 kbq/ $\mu$ L) for  $^{68}\text{Ga}$  labelled SiNPs (Figure 3 A-B), with  
200 theoretical limits for isotopes tested here in SWIR CLI shown in Table 1.(42)

201 Next, the tissue SWIR CLI detection limit was assessed. A euthanized mouse received 30  $\mu$ l  
202 respective paw injections of varying  $^{68}\text{Ga}$ -SiNPs activities. As can be seen in Figure 3C–D,  $^{68}\text{Ga}$ -  
203 SiNPs were detected via SWIR CLI at 403.3 kbq, within clinically administered levels (~148  
204 Mbq).(49)

### 205 ***In vivo* Detection of Radioisotope SWIR CLI**

206  $^{90}\text{Y}$  conjugated to SiNPs was used for *in vivo* SWIR CLI radioisotope detection.(38)  $^{90}\text{Y}$  has  
207 been shown to improve the SNR of CL detection over e.g.  $^{18}\text{F}$  or  $^{68}\text{Ga}$  due to reduced  $\gamma$  sensor  
208 strikes.(50) The long exposure times for SWIR CLI contaminated the SWIR CL image with  
209 thermal signatures (removed in post processing via rolling ball background subtraction),  
210 complicating SWIR CLI over VIS CLI. Mice were injected with ~7.4 Mbq of  $^{90}\text{Y}$  labeled SiNPs into  
211 a single footpad and imaged 3 hours later.  $^{90}\text{Y}$  is administered clinically for radioembolization at  
212 activities ranging from 500 to 5291 Mbq.(47,48) The resulting SWIR CLI signal was readily  
213 detected over background thermal signatures present *in vivo* (n = 4 mice; Figure 4 and  
214 Supplemental Figure 6). Footpad injected radiolabeled SiNPs slowly migrate through the  
215 lymphatic system (48 hrs) preventing CL contamination of the endogenous thermal signature.(38)  
216 Respective residual thermal signatures remaining post background subtraction from each mouse  
217 were used to divide the image producing measurements in terms of signal to thermal background  
218 ratio (SBR; Supplemental Figure 2). SBRs from injected mice ranged from 1.68 to 4.63 with a  
219 mean of 3.07, see Figure 4B.

### 220 **DISCUSSION**

221 This work aimed to detect the theoretical SWIR CL emission from clinical radioisotopes via  
222 commercially available components (Supplemental Figure 7). To date SWIR CL has only been  
223 detected from LINAC sources which produce an order of magnitude brighter CL.(25,28) The  
224 devised setup and enclosure provided ambient light-free imaging.(51,52) The state of the art TEC  
225 SWIR sensors used in our study produces 2 to 3 orders of magnitude higher dark noise compared  
226 to EMCCD-based cameras. This intrinsic noise within the SWIR setup, an obstacle not only for  
227 SWIR CLI, has been the main limiting factor throughout this work.(53) In addition, the even further  
228 reduced light output at longer wavelengths necessitated longer exposure times (minutes versus  
229 seconds for VIS CLI). Nevertheless, the six radioisotopes we explored produced detectable SWIR  
230 CL (Figure 1), with relative radiances in line with VIS CLI.(3,41,42) SWIR CLI performed linearly  
231 with radioisotope levels (Figures 1, and 3). SWIR CLI radioisotope sensitivity was found to be 259  
232 kbq (8.51 kbq/ $\mu$ L) *in vitro* and 403.3 kbq in tissue with  $^{68}\text{Ga}$ . VIS CLI is four orders of magnitude  
233 more sensitive, with  $^{68}\text{Ga}$  detection reported at 0.00333 kbq/ $\mu$ L.(54) The insensitivity of SWIR CLI  
234 limits applications with the current generation of SWIR cameras. However, its advantage of  
235 reduced scattering in combination with the increased transmission of CL in the SWIR region  
236 (Figure 2 and Supplemental Figure 7), potentially paired with SWIR-void room lighting, could open  
237 new applications for SWIR CLI (28) that benefit from improved radioisotope resolution at depth.  
238 Combining the strengths of InGaAs (900 – 1700 nm) and silicon (400 – 900 nm) based sensors  
239 would open further applications for CLI and is worth investigating.(16,19,46,55,56). Assuming  
240 sufficient radioisotope levels, SWIR CLI can be performed close to video rates (0.25s; Figure 1).

241 The detected radioisotope SWIR CL spectrum was found to be in line with the SWIR LINAC  
242 spectrum.(28) Similarly to SWIR LINAC CL, detection of theoretically emitted CL above 1400 nm

248 could not be reliably detected likely due to sensor noise and water absorption (Supplemental  
249 Figure 7). However, the advantage of wavelengths above 1400 compared to 900-1300 nm is  
250 unclear for SWIR CLI in any case due to the increased absorption of water above 1300  
251 nm.(19,46).

252  
253 The preclinical applicability of SWIR CL was investigated and initially focused on the *ex vivo*  
254 SWIR CLI of intratumorally injected  $^{18}\text{F}$ -FDG, see Supplemental Figure 3.  $^{18}\text{F}$ 's weak CL (26x  
255 dimmer than  $^{68}\text{Ga}$ ) required one hour acquisition times for accurate signal detection.(42,54)  $^{90}\text{Y}$   
256 was used to overcome the limitations of  $^{68}\text{Ga}$  and  $^{18}\text{F}$  for this investigation (very little  $\gamma$  emission,  
257 brighter CL, longer half-life than  $^{68}\text{Ga}$ , 64.2 hrs vs 1.13 hrs).(2,41)  $^{90}\text{Y}$  labeled SiNPs were injected  
258 into the footpad of live mice for *in vivo* SWIR CLI detection.(38) Mice were imaged 3 hours post  
259 injection (~7.4 Mbq of  $^{90}\text{Y}$ -SiNPs) together with a non-injected control mouse. Exposure times of  
260 15 mins provided a reliable SWIR CL signal that was detected over endogenous thermal signature  
261 and inherent noise, see Figure 4.

262

## 263 CONCLUSION

264

265 Our study presents the first example and proof of principle of *in vivo* radioisotope SWIR CLI  
266 detection. Considering the optical properties of tissue it has been shown that the majority of CL  
267 emitted from tissue at depth is above 600 nm.(3,16) Therefore, the ideal radioisotope CL camera  
268 would be one that combines the spectral range of thinned SWIR sensors (600 – 1700 nm) with  
269 the photon sensitivity of EMCCD based sensors. Future iterations of SWIR CLI should aim to  
270 tackle its main limitations via a faster lens and dark noise reduced camera sensor to improve  
271 overall sensitivity along with lead shielding to further increase sensitivity via  $\gamma$  strike reduction.  
272 Such components would be highly custom and outside the scope of this proof of principle work.  
273 Human eyes respond to light from ~400 to ~700 nm and by changing ambient lighting to non-  
274 SWIR emitting LEDs, radioisotope SWIR CLI could be performed in a well lit room and without  
275 the need for a dark enclosure, as achieved for LINAC CLI.(7,30) This would directly impact  
276 preclinical CLI which is a common, fast and cost-effective PET alternative for novel radiotracers  
277 and treatment tracking.(57,58) However, significant improvements are required in SWIR optics  
278 and technology before this can be realized.

279

280

## 281 ACKNOWLEDGMENTS

282

283 Many thanks to: Craig Wall, Manjul Shah, Sabbir Liakat and Princeton Teledyne for the  
284 NIRvana 640 TE camera and lens and Photon Etc. for the Zephir 1.7x camera. Sincere thanks  
285 to Valerie Longo and Pat Zanzonico of MSKCC. Funding was provided by the National Institutes  
286 of Health NCI grants R01CA183953 (to Jan Grimm) and P30 CA08748 (to Craig  
287 Thompson/MSKCC).

288

## 289 Author Contributions

290

291 BML: system setup, experiment design and execution, imaging and analysis. QZ: SiNP  
292 radiolabeling. MS, EI, HH and AO: aided *in vivo* experiments. BML, ECP and JG: study design.  
293 All authors: experimental setup, experimental procedures, data interpretation and presentation  
294 and manuscript writing. The authors declare no conflicts of interest.

295

296 **KEY POINTS**

297

298 This is the first work to show SWIR CLI (900 – 1700 nm) from radioisotopes which has so far  
299 only been detected from LINACs, orders of magnitude brighter.

300

301 This work detected SWIR CLI via commercially available components from numerous  
302 pre/clinical radioisotopes with the radiances and spectrum performing in a manner contiguous  
303 with VIS CLI (400 – 900 nm).

304

305 SWIR CLI has distinct advantages over VIS CLI in terms of reduced scattering and absorption  
306 at depth however, significant technological and optical improvements are required for  
307 comparable sensitivity.

308

309 **REFERENCES**

310  
311  
312  
313  
314  
315  
316  
317  
318  
319  
320  
321  
322  
323  
324  
325  
326  
327  
328  
329  
330  
331  
332  
333  
334  
335  
336  
337  
338  
339  
340  
341  
342  
343  
344  
345  
346  
347  
348  
349  
350  
351  
352

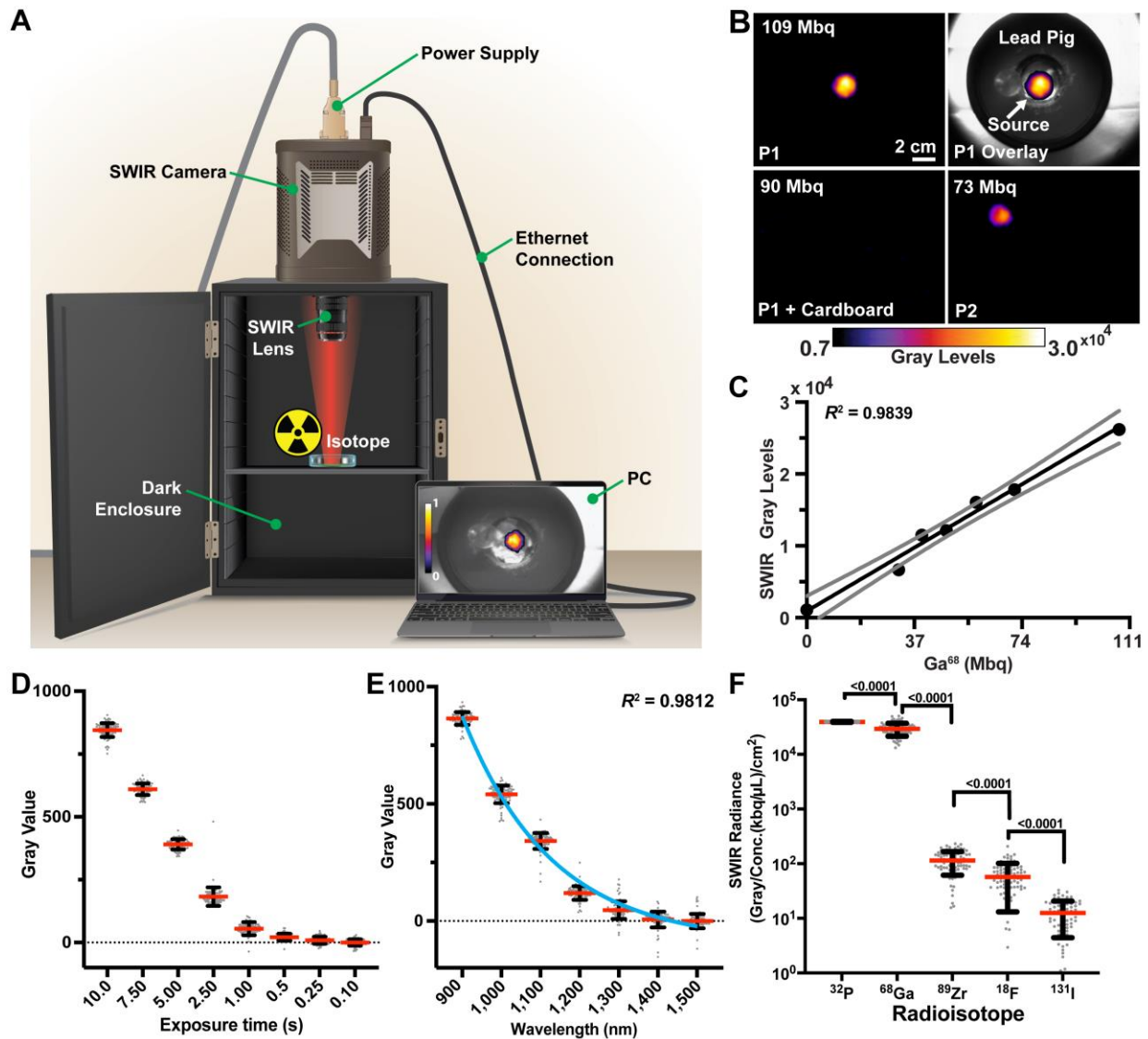
1. Čerenkov P. Visible light from pure liquids under the impact of  $\gamma$ -rays. Paper presented at: CR (Dokl.) Acad. Sci. URSS, 1934.
2. Ciarrocchi E, Belcari N. Cerenkov luminescence imaging: physics principles and potential applications in biomedical sciences. *EJNMMI physics*. 2017;4:1-31.
3. Glaser AK, Zhang R, Andreozzi JM, Gladstone DJ, Pogue BW. Cherenkov radiation fluence estimates in tissue for molecular imaging and therapy applications. *Physics in Medicine & Biology*. 2015;60:6701.
4. Ruggiero A, Holland JP, Lewis JS, Grimm J. Cerenkov luminescence imaging of medical isotopes. *Journal of Nuclear Medicine*. 2010;51:1123-1130.
5. Contalbrigo M, Kubarovskiy V, Mirazita M, et al. The CLAS12 ring imaging Cherenkov detector. *Nuclear Instruments and Methods in Physics Research Section A: Accelerators, Spectrometers, Detectors and Associated Equipment*. 2020:163791.
6. Mitchell GS, Gill RK, Boucher DL, Li C, Cherry SR. In vivo Cerenkov luminescence imaging: a new tool for molecular imaging. *Philosophical Transactions of the Royal Society A: Mathematical, Physical and Engineering Sciences*. 2011;369:4605-4619.
7. Pratt EC, Skubal M, Mc Larney B, et al. Prospective testing of clinical Cerenkov luminescence imaging against standard-of-care nuclear imaging for tumour location. *Nature Biomedical Engineering*. 2022:1-10.
8. Tamura R, Pratt EC, Grimm J. Innovations in nuclear imaging instrumentation: Cerenkov imaging. Paper presented at: Seminars in nuclear medicine, 2018.
9. Miao T, Bruza P, Pogue BW, et al. Cherenkov imaging for linac beam shape analysis as a remote electronic quality assessment verification tool. *Medical physics*. 2019;46:811-821.
10. D'Souza JW, Hensley H, Doss M, et al. Cerenkov luminescence imaging as a modality to evaluate antibody-based PET radiotracers. *Journal of Nuclear Medicine*. 2017;58:175-180.
11. Lohrmann C, Zhang H, Thorek DL, et al. Cerenkov luminescence imaging for radiation dose calculation of a  $^{90}\text{Y}$ -labeled gastrin-releasing peptide receptor antagonist. *Journal of Nuclear Medicine*. 2015;56:805-811.
12. Olde Heuvel J, de Wit-van der Veen BJ, van der Poel HG, et al. ( $^{68}\text{Ga}$ )-PSMA Cerenkov luminescence imaging in primary prostate cancer: first-in-man series. *European journal of nuclear medicine and molecular imaging*. 2020;47:2624-2632.

- 353 **13.** Thorek DL, Riedl CC, Grimm J. Clinical Cerenkov luminescence imaging of 18F-FDG. *Journal*  
354 *of Nuclear Medicine*. 2014;55:95-98.  
355
- 356 **14.** Grootendorst MR, Cariati M, Pinder SE, et al. Intraoperative assessment of tumor  
357 resection margins in breast-conserving surgery using 18F-FDG Cerenkov luminescence imaging:  
358 a first-in-human feasibility study. *Journal of Nuclear Medicine*. 2017;58:891-898.  
359
- 360 **15.** Jarvis LA, Zhang R, Gladstone DJ, et al. Cherenkov Video Imaging Allows for the First  
361 Visualization of Radiation Therapy in Real Time. *International Journal of Radiation*  
362 *Oncology\*Biography\*Physics*. 2014;89:615-622.  
363
- 364 **16.** Jacques SL. Optical properties of biological tissues: a review. *Physics in Medicine &*  
365 *Biology*. 2013;58:R37.  
366
- 367 **17.** Yaroshevsky A, Glasser Z, Granot Ee, Sternklar S. Transition from the ballistic to the  
368 diffusive regime in a turbid medium. *Optics letters*. 2011;36:1395-1397.  
369
- 370 **18.** Ding F, Zhan Y, Lu X, Sun Y. Recent advances in near-infrared II fluorophores for  
371 multifunctional biomedical imaging. *Chemical science*. 2018;9:4370-4380.  
372
- 373 **19.** Cao Q, Zhegalova NG, Wang ST, Akers WJ, Berezin MY. Multispectral imaging in the  
374 extended near-infrared window based on endogenous chromophores. *Journal of biomedical*  
375 *optics*. 2013;18:101318.  
376
- 377 **20.** Thorek DL, Ogirala A, Beattie BJ, Grimm J. Quantitative imaging of disease signatures  
378 through radioactive decay signal conversion. *Nature medicine*. 2013;19:1345.  
379
- 380 **21.** Zhang Q, Pratt EC, Tamura R, et al. Ultrasmall Downconverting Nanoparticle for Enhanced  
381 Cerenkov Imaging. *Nano Letters*. 2021;21:4217-4224.  
382
- 383 **22.** Pratt EC, Shaffer TM, Zhang Q, Drain CM, Grimm J. Nanoparticles as multimodal photon  
384 transducers of ionizing radiation. *Nature nanotechnology*. 2018;13:418-426.  
385
- 386 **23.** Thimsen E, Sadtler B, Berezin MY. Shortwave-infrared (SWIR) emitters for biological  
387 imaging: a review of challenges and opportunities. *Nanophotonics*. 2017;6:1043-1054.  
388
- 389 **24.** Carr JA, Franke D, Caram JR, et al. Shortwave infrared fluorescence imaging with the  
390 clinically approved near-infrared dye indocyanine green. *Proceedings of the National Academy of*  
391 *Sciences*. 2018;115:4465-4470.  
392
- 393 **25.** Naczynski DJ, Sun C, Türkcan S, et al. X-ray-induced shortwave infrared biomedical  
394 imaging using rare-earth nanoprobables. *Nano letters*. 2015;15:96-102.  
395

- 396 **26.** Cao X, Jiang S, Jia MJ, et al. Cherenkov excited short-wavelength infrared fluorescence  
397 imaging in vivo with external beam radiation. *Journal of biomedical optics*. 2018;24:051405.  
398
- 399 **27.** Dothager RS, Goiffon RJ, Jackson E, Harpstrite S, Piwnica-Worms D. Cerenkov radiation  
400 energy transfer (CRET) imaging: a novel method for optical imaging of PET isotopes in biological  
401 systems. *PLoS one*. 2010;5:e13300.  
402
- 403 **28.** Cao X, Jiang S, Jia M, et al. Observation of short wavelength infrared (SWIR) Cherenkov  
404 emission. *Optics letters*. 2018;43:3854-3857.  
405
- 406 **29.** Glaser AK, Zhang R, Gladstone DJ, Pogue BW. Optical dosimetry of radiotherapy beams  
407 using Cherenkov radiation: the relationship between light emission and dose. *Physics in Medicine  
408 & Biology*. 2014;59:3789.  
409
- 410 **30.** Glaser AK, Zhang R, Davis SC, Gladstone DJ, Pogue BW. Time-gated Cherenkov emission  
411 spectroscopy from linear accelerator irradiation of tissue phantoms. *Optics Letters*.  
412 2012;37:1193-1195.  
413
- 414 **31.** Browne E. Commonly used radioactive sources. *The European Physical Journal C, Particles  
415 and Fields*. 2000;15:190-190.  
416
- 417 **32.** Pritychenko B, Běťák E, Kellett M, Singh B, Totans J. The nuclear science references (NSR)  
418 database and web retrieval system. *Nuclear Instruments and Methods in Physics Research Section  
419 A: Accelerators, Spectrometers, Detectors and Associated Equipment*. 2011;640:213-218.  
420
- 421 **33.** Tendler II, Hartford A, Jermyn M, et al. Experimentally observed cherenkov light  
422 generation in the eye during radiation therapy. *International Journal of Radiation Oncology\*  
423 Biology\* Physics*. 2020;106:422-429.  
424
- 425 **34.** Huang Y-H, Yang C-C, Peng T-C, et al. 10-Gb/s InGaAs pin photodiodes with wide spectral  
426 range and enhanced visible spectral response. *IEEE Photonics Technology Letters*. 2007;19:339-  
427 341.  
428
- 429 **35.** Elvidge CD, Keith DM, Tuttle BT, Baugh KE. Spectral identification of lighting type and  
430 character. *Sensors*. 2010;10:3961-3988.  
431
- 432 **36.** Schindelin J, Arganda-Carreras I, Frise E, et al. Fiji: an open-source platform for biological-  
433 image analysis. *Nature methods*. 2012;9:676-682.  
434
- 435 **37.** Walter J. FFT-filter. Available at: <http://rsbinfo.nih.gov/ij/plugins/fft-filter.html>. 2001.  
436
- 437 **38.** Shaffer TM, Wall MA, Harmsen S, et al. Silica nanoparticles as substrates for chelator-free  
438 labeling of oxophilic radioisotopes. *Nano letters*. 2015;15:864-868.  
439

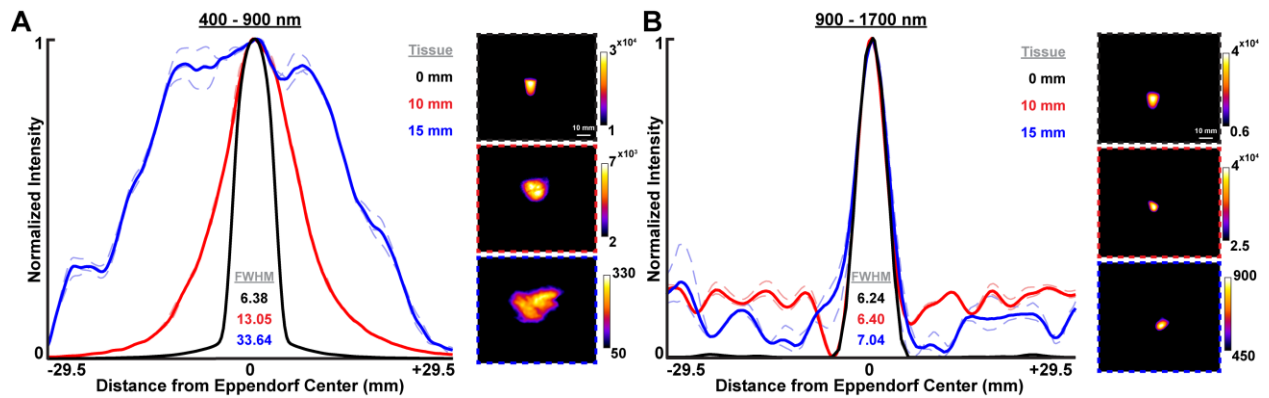
- 440 **39.** Darr C, Harke NN, Radtke JP, et al. Intraoperative 68Ga-PSMA Cerenkov luminescence  
441 imaging for surgical margins in radical prostatectomy: a feasibility study. *Journal of Nuclear*  
442 *Medicine*. 2020;61:1500-1506.
- 443
- 444 **40.** Banerjee SR, Pomper MG. Clinical applications of Gallium-68. *Applied Radiation and*  
445 *Isotopes*. 2013;76:2-13.
- 446
- 447 **41.** Beattie BJ, Thorek DL, Schmidlein CR, Pentlow KS, Humm JL, Hielscher AH. Quantitative  
448 modeling of Cerenkov light production efficiency from medical radionuclides. *PloS one*.  
449 2012;7:e31402.
- 450
- 451 **42.** Gill RK, Mitchell GS, Cherry SR. Computed Cerenkov luminescence yields for radionuclides  
452 used in biology and medicine. *Physics in Medicine & Biology*. 2015;60:4263.
- 453
- 454 **43.** Martin T, Dixon P. InGaAs sees infrared and visible light. *Laser focus world*. 2004;40:109-  
455 111.
- 456
- 457 **44.** Williamson JB, Carey KW, Kellert F, Braum D, Hodge L, Loncasty D. High-density, planar  
458 Zn-diffused InGaAs/InP photodetector arrays with extended short-wavelength response. *IEEE*  
459 *Transactions on Electron Devices*. 1991;38:2707.
- 460
- 461 **45.** Hoelter TR, Barton JB. Extended short-wavelength spectral response from InGaAs focal  
462 plane arrays. Paper presented at: Infrared Technology and Applications XXIX, 2003.
- 463
- 464 **46.** Carr JA, Aellen M, Franke D, So PT, Bruns OT, Bawendi MG. Absorption by water increases  
465 fluorescence image contrast of biological tissue in the shortwave infrared. *Proceedings of the*  
466 *National Academy of Sciences*. 2018;115:9080-9085.
- 467
- 468 **47.** Kim SP, Cohalan C, Kopek N, Enger SA. A guide to 90Y radioembolization and its dosimetry.  
469 *Physica Medica*. 2019;68:132-145.
- 470
- 471 **48.** Fidelman N, Kerlan Jr RK, Hawkins RA, et al. Radioembolization with 90Y glass  
472 microspheres for the treatment of unresectable metastatic liver disease from chemotherapy-  
473 refractory gastrointestinal cancers: final report of a prospective pilot study. *Journal of*  
474 *gastrointestinal oncology*. 2016;7:860.
- 475
- 476 **49.** Demirci E, Toklu T, Yeyin N, et al. Estimation of the organ absorbed doses and effective  
477 dose from 68Ga-PSMA-11 PET scan. *Radiation protection dosimetry*. 2018;182:518-524.
- 478
- 479 **50.** Carpenter CM, Ma X, Liu H, et al. Cerenkov luminescence endoscopy: improved molecular  
480 sensitivity with  $\beta^-$ -emitting radiotracers. *Journal of Nuclear Medicine*. 2014;55:1905-1909.
- 481
- 482 **51.** Alsheikh H. [P091] Investigation of cherenkov imaging using IVIS bioluminescence  
483 scanner. *Physica Medica: European Journal of Medical Physics*. 2018;52:127.

- 484  
485 **52.** Spinelli AE, Kuo C, Rice BW, et al. Multispectral Cerenkov luminescence tomography for  
486 small animal optical imaging. *Optics Express*. 2011;19:12605-12618.  
487  
488 **53.** Fraenkel R, Berkowicz E, Bikov L, et al. Development of low-SWaP and low-noise InGaAs  
489 detectors. Paper presented at: Infrared Technology and Applications XLIII, 2017.  
490  
491 **54.** de Wit-van der Veen B, Vyas K, Tuch D, Grootendorst M, Stokkel M, Slump C. Performance  
492 evaluation of Cerenkov luminescence imaging: a comparison of <sup>68</sup>Ga with <sup>18</sup>F. *EJNMMI physics*.  
493 2019;6:1-13.  
494  
495 **55.** Zhang H, Salo DC, Kim DM, Komarov S, Tai Y-C, Berezin MY. Penetration depth of photons  
496 in biological tissues from hyperspectral imaging in shortwave infrared in transmission and  
497 reflection geometries. *Journal of biomedical optics*. 2016;21:126006.  
498  
499 **56.** Golovynskyi S, Golovynska I, Stepanova LI, et al. Optical windows for head tissues in near-  
500 infrared and short-wave infrared regions: Approaching transcranial light applications. *Journal of*  
501 *biophotonics*. 2018;11:e201800141.  
502  
503 **57.** Xu Y, Chang E, Liu H, Jiang H, Gambhir SS, Cheng Z. Proof-of-concept study of monitoring  
504 cancer drug therapy with Cerenkov luminescence imaging. *Journal of Nuclear Medicine*.  
505 2012;53:312-317.  
506  
507 **58.** Liu M, Zheng S, Zhang X, et al. Cerenkov luminescence imaging on evaluation of early  
508 response to chemotherapy of drug-resistant gastric cancer. *Nanomedicine: Nanotechnology,*  
509 *Biology and Medicine*. 2018;14:205-213.  
510  
511  
512



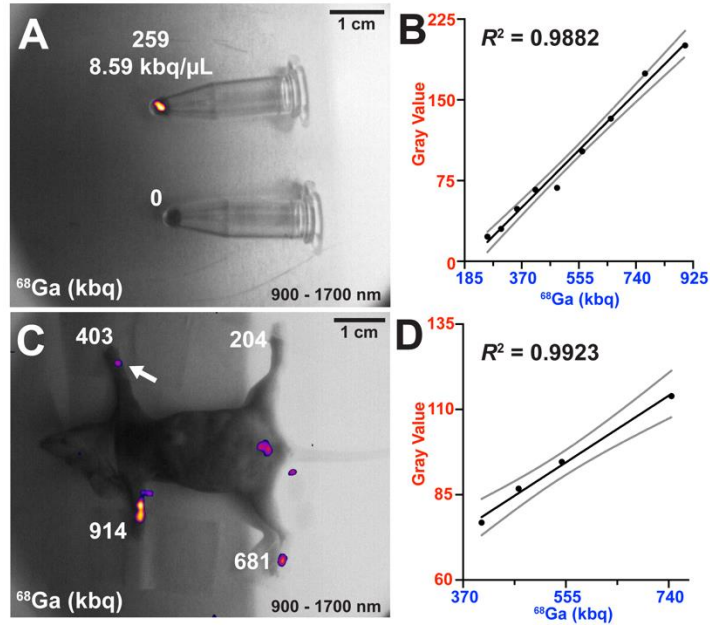
513  
514  
515  
516  
517  
518  
519  
520  
521  
522  
523  
524  
525  
526  
527  
528

**Figure 1. SWIR CL radioisotope imaging setup and characterization.** A) A dark enclosure was used for all imaging. 16mm or 8mm f/1.4 SWIR lens was mounted on the camera. ©2022 Memorial Sloan Kettering Cancer Center. All rights reserved. B) Linearity assessment of the camera via <sup>68</sup>Ga imaged at positions (P1, P2) across the FOV, P1 + Cardboard confirming detection was not a result of  $\gamma$  strikes. C) SWIR gray levels and corresponding <sup>68</sup>Ga activity (Mbq). Linear regression and 95% confidence intervals are shown, Pearson  $R^2 = 0.9839$  and two-tailed  $p$  value  $<0.0001$ . SWIR CLI is linearly responsive and quantitative as found with VIS CLI. D) <sup>32</sup>P SWIR gray value intensity in relation to exposure time changes E) Graphical representation of the radioisotope (<sup>32</sup>P) SWIR CL emission spectrum from 900 to 1500 nm, blue line: one phase exponential decay function,  $R^2 = 0.9812$ . Inherent system noise, low photon production and water absorption prevents detection  $>1400$  nm. F) Descending radioisotope radiance (<sup>32</sup>P, <sup>68</sup>Ga, <sup>18</sup>F, <sup>89</sup>Zr and <sup>131</sup>I) corrected for concentration (kbq/ $\mu$ L) and spatial FOV. Students  $t$ -test (upaired, two-sided)  $p$  values are shown. In all cases, the mean (red line), standard deviation (black lines) and individual measurements ( $n = 90$  technical replicates, gray dots) are shown, excluding negative values.



529  
530  
531  
532  
533  
534  
535  
536  
537  
538

**Figure 2. Reduced scattering via SWIR CLI over VIS CLI** A) Left, Normalized VIS CLI (400 – 900 nm) line intensity profiles from the phantom setup. FWHMs increase with scattering tissue depth at 0, 10 and 15 mm with respective FWHMs of 6.38, 13.05 and 33.64 mm. Right, representative VIS CLI images. B) Left, Normalized SWIR CLI line intensity profiles of  $^{90}\text{Y}$  (Eppendorf, 55.5 Mbq in 200  $\mu\text{L}$  of saline) at increasing scattering tissue (chicken breast: 0, 10 and 15 mm), full width half maximums (FWHM) of 6.24, 6.40 and 7.04 mm. Right, representative SWIR CL images. In all cases three separate line measurements are made from the images at each depth (dotted lines) with the mean shown (solid line).



539  
 540  
 541  
 542  
 543  
 544  
 545  
 546  
 547  
 548

**Figure 3. In vitro and ex vivo SWIR CLI radioisotope sensitivity limit for <sup>68</sup>Ga radiolabeled SiNPs.** A) SWIR CLI radioisotope in vitro detection limit for <sup>68</sup>Ga-SiNPs post multiple half-lives. B) SWIR CLI decay tracking to the limit of detection linear regression (solid black line, R<sup>2</sup> = 0.9882) and 95% confidence intervals are shown (dotted gray lines). C) The ex vivo SWIR CLI (900 – 1700 nm) limit of detection for <sup>68</sup>Ga labeled SiNPs. The detection limit slightly worsens in tissue compared to in vitro imaging (~140 kbq less sensitive). D) Linear regression analysis (R<sup>2</sup> = 0.9923) of the ex vivo SWIR CLI of the <sup>68</sup>Ga labeled SiNPs to the limit of detection (403.3 kbq, C) paw labeled with white arrow.

549  
550  
551  
552  
553  
554  
555

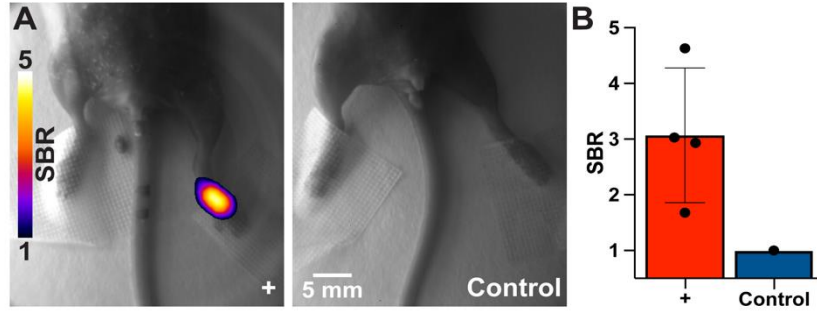
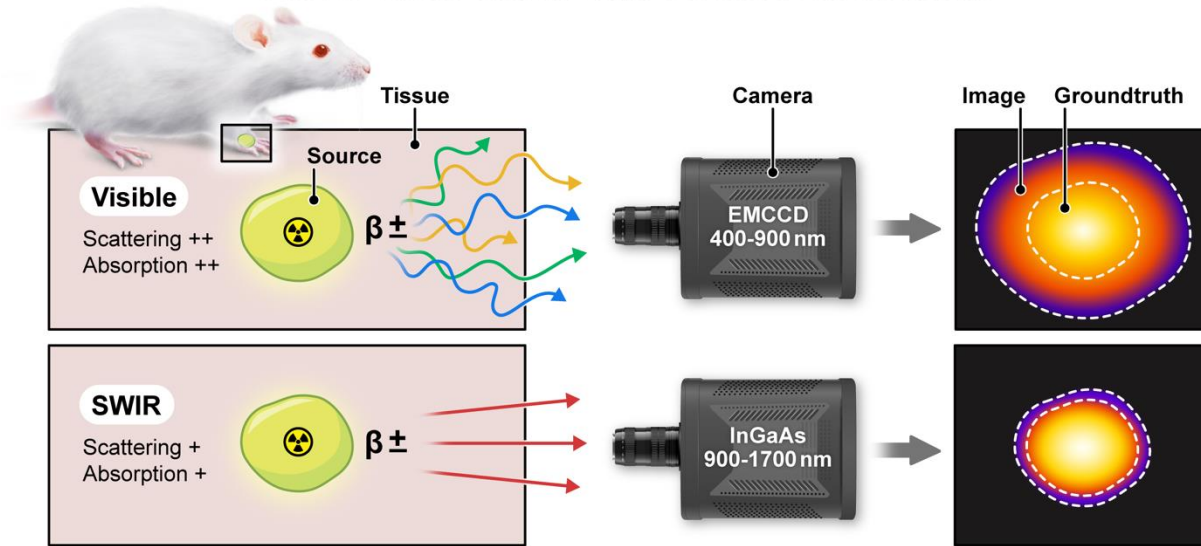


**Figure 4. In vivo SWIR CLI detection of  $^{90}\text{Y}$  labeled SiNPs three hours post injection into the footpad** A) Left, Representative images of a mouse injected (+) with  $^{90}\text{Y}$  labeled SiNPs (~7.4 Mbq). Right, image of a control mouse without any injection. C) Quantified SBR values of injected ( $n = 4$ ) vs control mice ( $n = 1$ ). All images are shown in respective signal to background ratios (SBR).

## SWIR vs Visible Radioisotope Cerenkov Luminescence



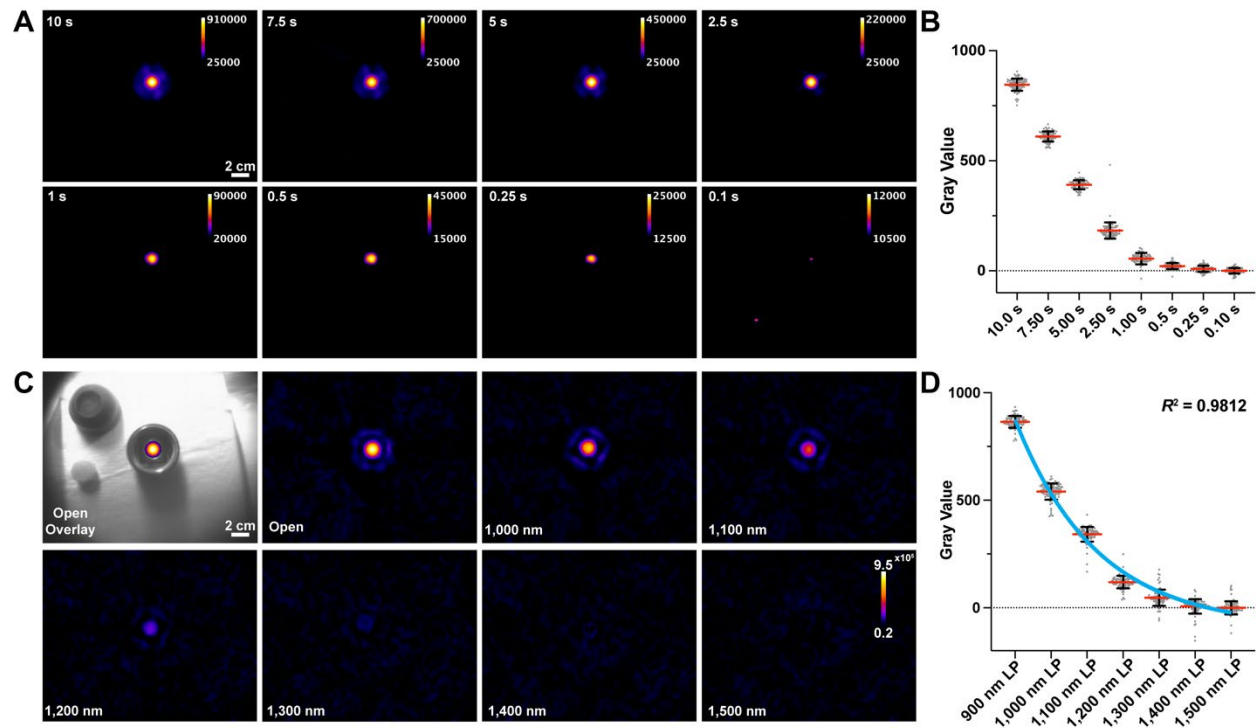
556  
557

**Graphical Abstract** ©2022 Memorial Sloan Kettering Cancer Center. All rights reserved.

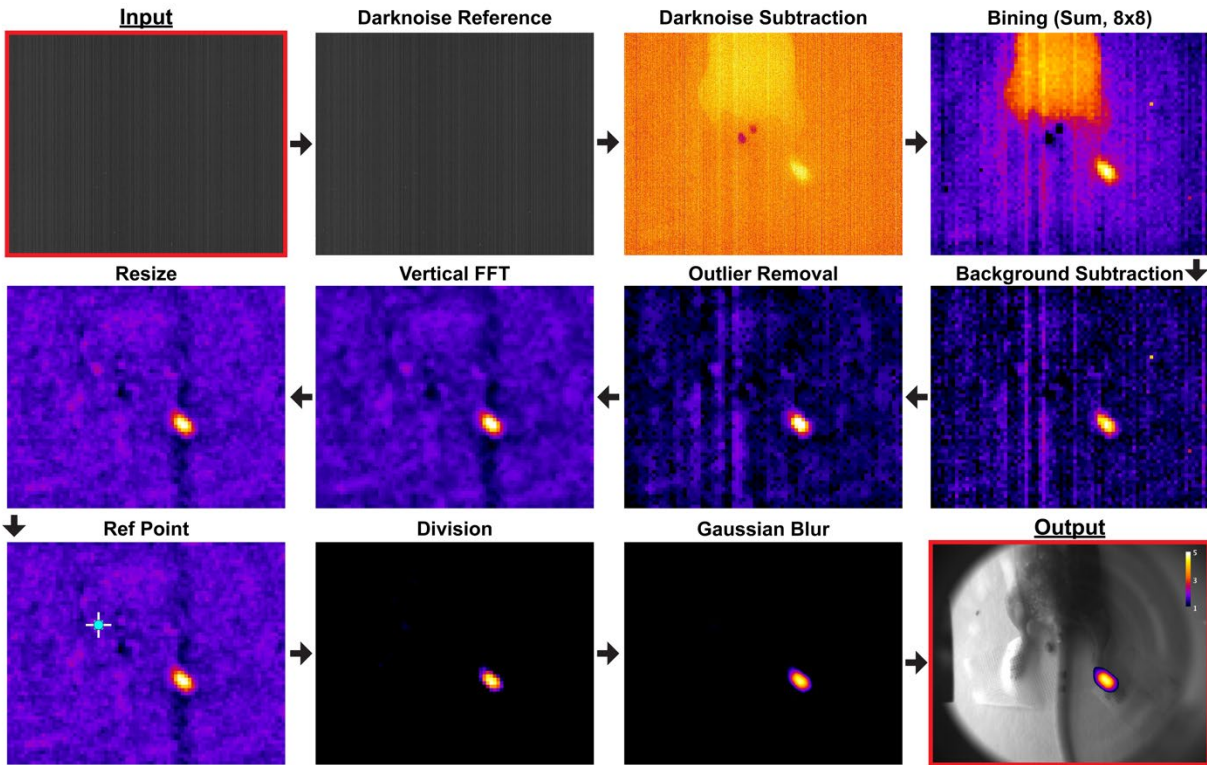
## Supplemental Material: Shortwave infrared detection of medical radioisotope Cerenkov luminescence

Benedict E. Mc Larney<sup>1,2</sup>, Qize Zhang<sup>1,2</sup>, Edwin C. Pratt<sup>1,2</sup>, Magdalena Skubal<sup>1,2</sup>, Elizabeth Isaac<sup>1,2</sup>, Hsiao-Ting Hsu<sup>1,2</sup>, Anuja Ogirala<sup>1,2</sup>, Jan Grimm<sup>1,2,3,4,5,\*</sup>

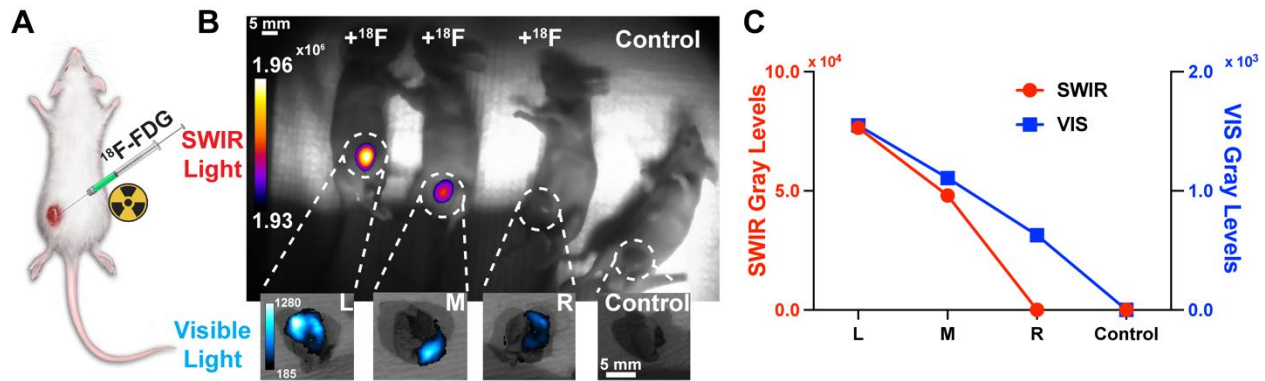
1. Molecular Pharmacology Program, Memorial Sloan Kettering Cancer Center, New York, NY, USA
  2. Molecular Imaging Therapy Service, Memorial Sloan Kettering Cancer Center, New York, NY, USA
  3. Pharmacology Program, Weill Cornell Medical College, New York, NY USA
  4. Department of Radiology, Memorial Sloan Kettering Cancer Center, New York, NY, USA
  5. Department of Radiology, Weill, Cornell Medical Center, New York, NY, USA
- \* . Corresponding author: Jan Grimm - [grimmj@mskcc.org](mailto:grimmj@mskcc.org)



**Supplemental Figure 1. SWIR CLI radioisotope temporal detection limit and emission spectrum** A) Representative SWIR CL images at varying exposure times. SWIR CL was detected at acquisition speeds of up to 0.25s. B) Gray value intensity in relation to exposure time changes C) The SWIR CL emission spectrum of <sup>32</sup>P is shown D) Graphical representation of the radioisotope SWIR CL emission spectrum from 900 to 1500 nm, the line represents a one phase exponential decay function,  $R^2 = 0.9812$ . Inherent system noise, low photon production and water absorption prevents detection >1400 nm. A) and C) each panel comprises the summation of  $n = 90$  technical replicates. B) and D) each replicate (gray dots,  $n = 90$ , technical), mean (red line) and standard deviation (black lines) are shown.

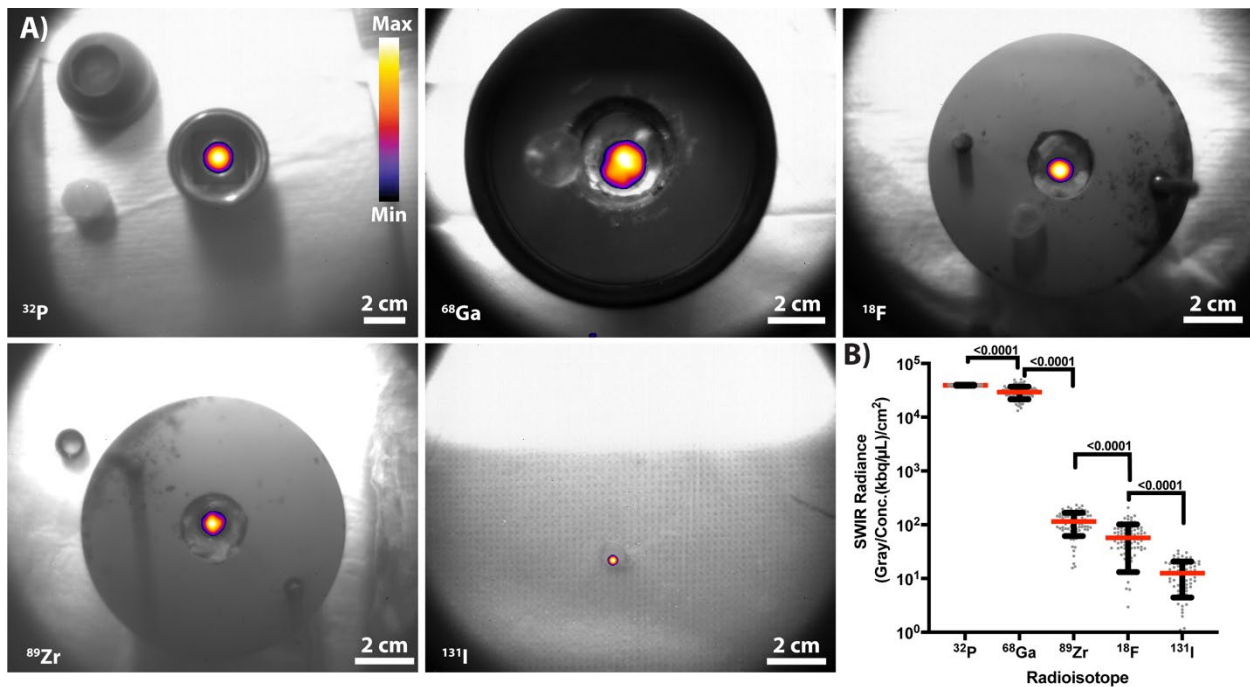


**Supplemental Figure 2. Image processing pipeline for *in vivo* SWIR CLI.** Images are presented from input to output including all necessary processing steps to generate the *in vivo* images. The input is based on a summation of  $n = 90$ , 16-bit, 10s images (900s/15 mins total acquisition time). Post darknoise subtraction images were processed in 32-bit formats. Rolling ball background subtraction was employed to remove endogenous thermal signal. Gaussian blur was applied with a sigma of 3.

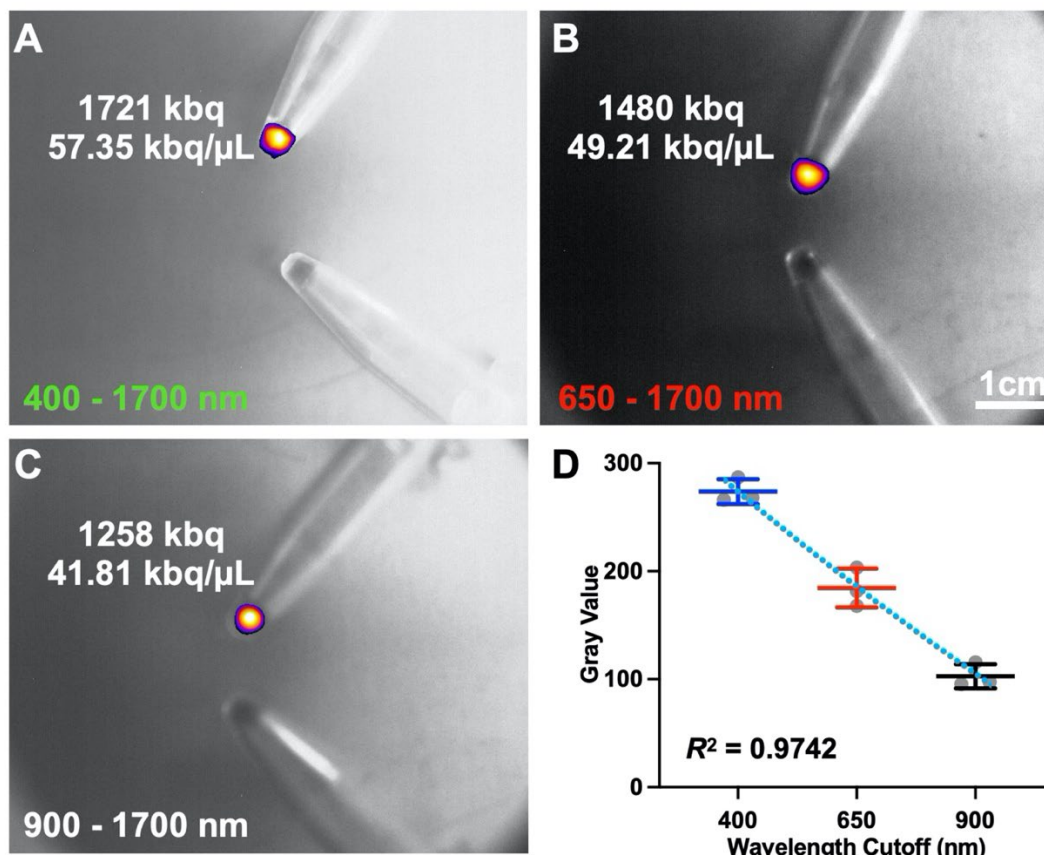


**Supplemental Figure 3. Ex vivo SWIR CLI and VIS CLI comparison of 4T1 xenografted mice intratumorally injected with clinical  $^{18}\text{F}$ -FDG** A) Euthanized mice were injected with  $^{18}\text{F}$ -FDG directly into the tumor. B) The corresponding image of 3 mice injected with  $^{18}\text{F}$ -FDG and one control mouse. Top, SWIR CL image, bottom VIS CL images of resected tumors (IVIS) C) Gray Value Cerenkov intensities for each tumor in both SWIR and visible light modalities (background subtracted). For B) and C) SWIR images and data points are summations from  $n = 360$  technical replicates and visible images are from a single acquisition from  $n = 3$   $^{18}\text{F}$ -FDG intratumorally injected mice and  $n = 1$  non-injected mouse (biological replicates).

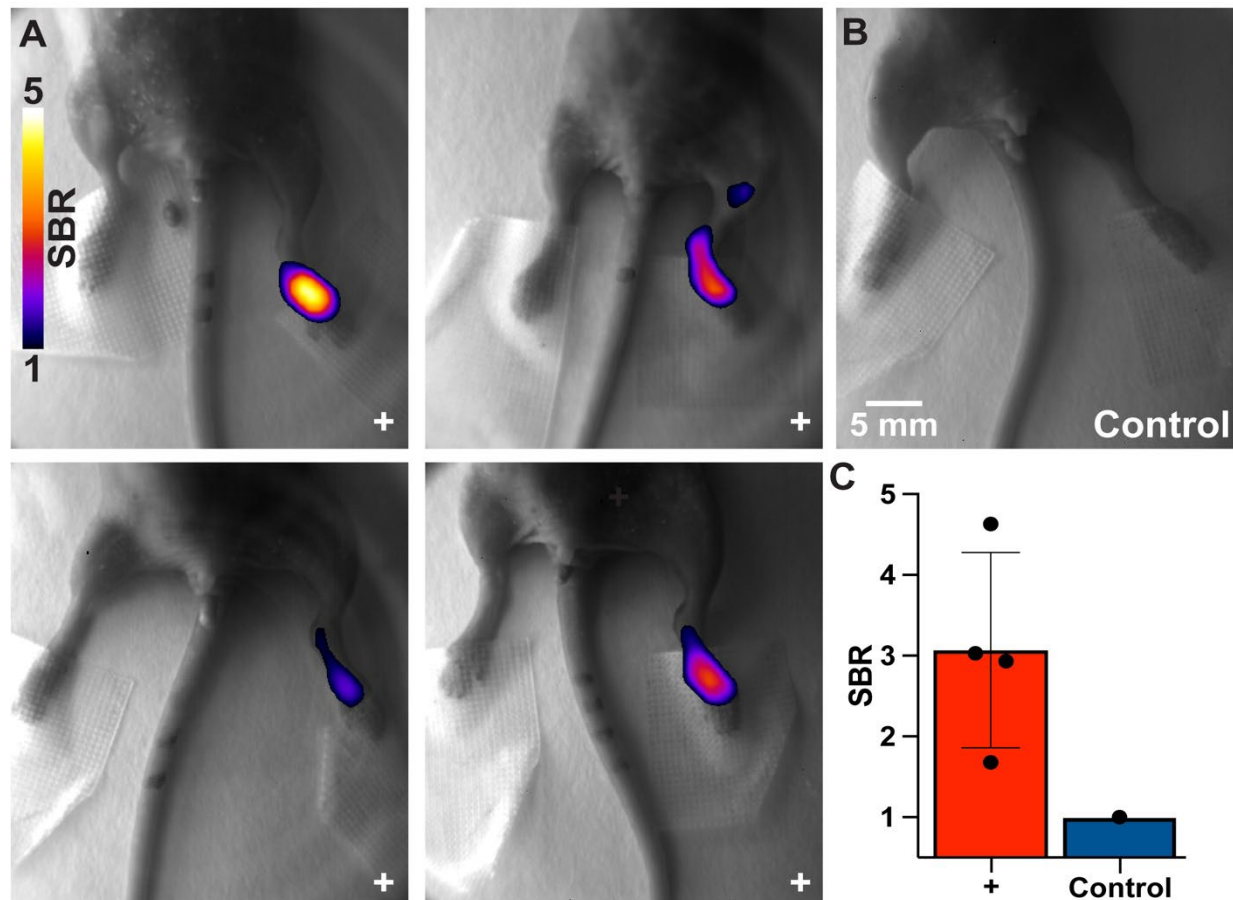
Initial experiments assessed the application of preclinical SWIR CLI with  $^{18}\text{F}$ -FDG. The inherent noise in the SWIR sensor and lower CL intensity of  $^{18}\text{F}$  ( $\beta$  average 0.25 MeV), required that  $^{18}\text{F}$ -FDG be injected on the order of a hundred Mbq to be detected in a murine setting. Experimentation in this format spatially concentrated the source further enabling detection (intratumoral injection, see Supplemental Figure 2A). It should be noted this is not representative of conventional CLI. Imaging was carried out post euthanasia and following the immediate injection of  $^{18}\text{F}$ -FDG into the tumor. As shown in Supplemental Figure 2B, three mice were administered  $^{18}\text{F}$ -FDG (with varying amounts up to 166.5 Mbq). The fourth mouse received no injection (negative control). Mice were imaged over the course of an hour (360 frames, 10s each) with SWIR CL detected in two mice. Tumors were resected post SWIR CLI and imaged on a conventional VIS CLI system (IVIS, 400 – 900 nm), see Supplemental Figure 2B, bottom row. The corresponding gray values are plotted for both modalities in Supplemental Figure 2C. In the case of the left (L), middle (M) and control (Control) mice the values are in close agreement.



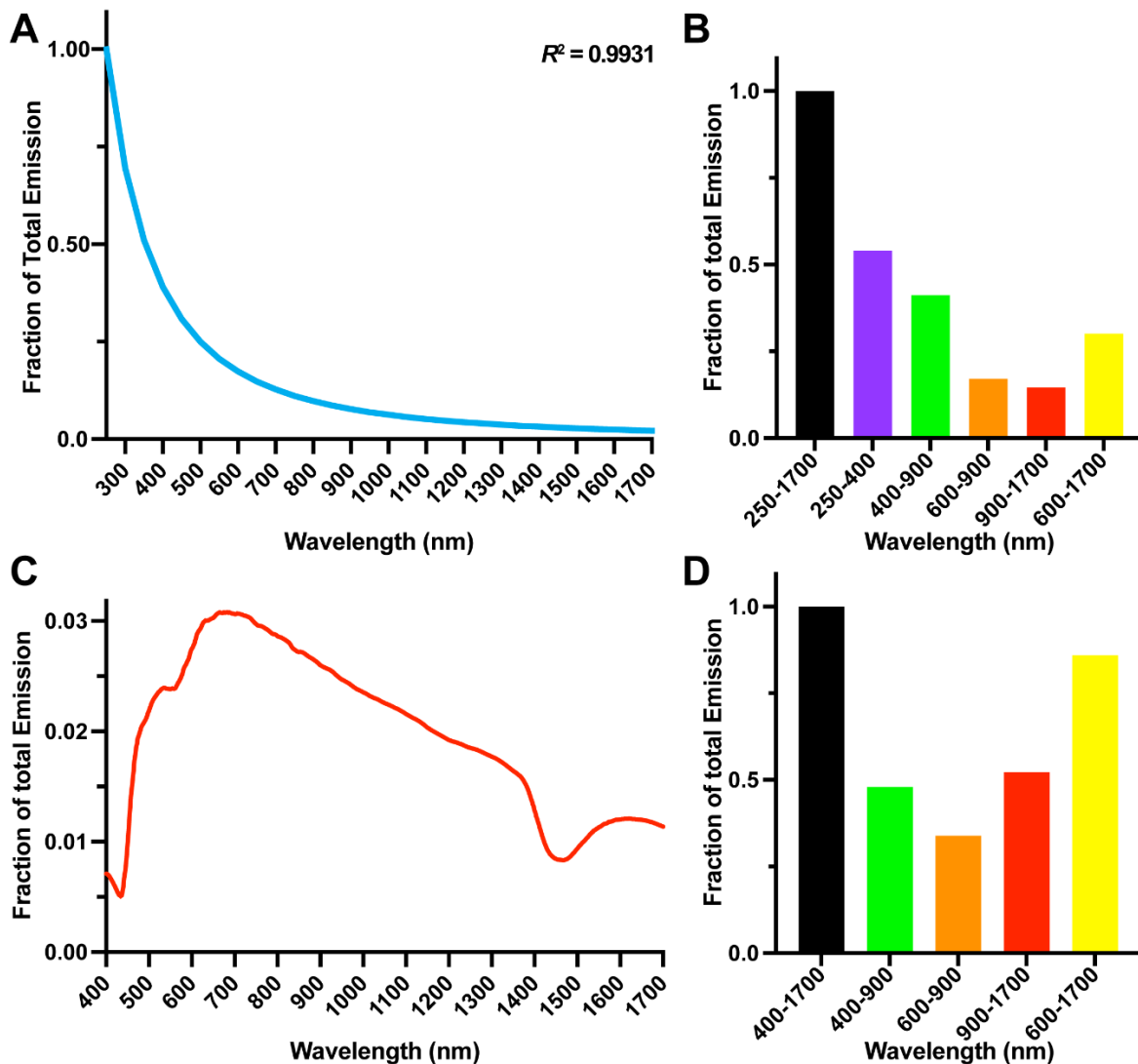
**Supplemental Figure 4. SWIR CLI of a variety of medical radioisotopes.** A) Representative SWIR CLI images for  $^{32}\text{P}$ ,  $^{68}\text{Ga}$ ,  $^{18}\text{F}$ ,  $^{89}\text{Zr}$  and  $^{131}\text{I}$ . Images are respectively thresholded and represents the summation of  $n = 90$  technical replicates. B) Descending radioisotope radiance corrected for concentration (Kbq/μL) and spatial FOV. Students t-test (upaired, two-sided)  $p$  values are shown. Mean (red line), standard deviation (black lines) and individual measurements ( $n = 90$  technical replicates, gray dots) are shown, excluding negative values.



**Supplementary Figure 5 SWIR CLI radioisotope localization for  $^{68}\text{Ga}$  radiolabeled SiNPs.** **A)** VIS-SWIR (400-1700 nm) image of  $^{68}\text{Ga}$ -SiNPs (Top) and non-radiolabeled SiNPs (Bottom). **B)** NIR-SWIR (650-1700 nm) image of the phantom as in A). **C)** SWIR (900-1700 nm) image of the phantom as in A). **D)** Decay corrected spectral emission profile of  $^{68}\text{Ga}$ -SiNPs, technical replicates (gray dots,  $n = 3$ ), median, SD and a fitted one phase exponential decay (dotted line,  $R^2 = 0.9742$ ) are shown.



**Supplemental Figure 6. In vivo SWIR CLI detection of  $^{90}\text{Y}$  labeled SiNPs three hours post injection into the footpad** **A)** Images of mice injected (+) with  $^{90}\text{Y}$  labeled SiNPs ( $\sim 7.4$  Mbq per mouse). **B)** Image of a control mouse without any injection. **C)** Quantified values of injected ( $n = 4$ ) vs control mice ( $n = 1$ ). All images are shown in respective signal to background ratios (SBR). A, Top left and Cntrl mouse are the same image as shown in Main Figure 4.



**Supplemental Figure 7. Theoretical Frank-Tamm Cerenkov emission from 250 – 1700 nm with and without absorption in terms of detector responses (400 – 1700 nm). A)** The exponential decay of light produced by Cerenkov emission calculated from 250 – 1700 nm. The emission decreases at a rate of  $1/\lambda^2$  with theoretical emission to 1700nm. The  $R^2$  value represents the goodness of fit for an exponential one phase decay. **B)** The fraction of theoretical light emitted at each of the relevant bands used in this work. Firstly the entire emission for both EMCCDs (silicon based) and SWIR (InGaAs based). Secondly the 250 – 400 nm band (UV) of which the EMCCD is not sensitive totalling 0.54 of the light. The 400 – 900 nm band, EMCCDs responsive wavelengths, totalling 0.411 of the emitted light. The 600 – 900 nm band, which represents the majority of the emission of CL from tissue detected by EMCCDs comprises 0.171 of the light and the 900 – 1700 nm band (SWIR) totalling 0.146 of the emitted light. Finally the 600 – 1700 nm band which represents the gross total theoretical CL emission from tissue totalling 0.301 of the light. **C)** The theoretical CL emission in terms of the optical transmission of tissue within the spectral response of the detectors used in this work (400 – 1700 nm). The optical transmission of 1mm of rat cortex was used as a reference.[40,41] Notable transmission losses are present between 400 – 600 nm due to hemoglobin absorption and at 1380 – 1590 nm due to water absorption. **D)** The normalized CL emission detection spectrum across similar bands as those in

B. When incorporating tissue transmission the 400 - 900 nm band captures 0.48 of the total light, 600 - 900 nm band captures 0.34. Interestingly the 900 - 1700 nm band captures 0.52 of the emitted CL and the 600 - 1700 nm band captures 0.86 of the total light. This highlights the advantage of SWIR CL imaging in tissue and also the recommended development of sensors with extended range to capture the 600 - 1700 nm spectrum. Note this data does not incorporate the true spectral response of EMCCDs or SWIR sensors and assumes 100% quantum efficiency in the relevant bands. The data does also not account for the inherent noise of either detectors nor the optical losses of respective VIS and SWIR lenses.

<b>Radioisotope</b>	<b>Total Photon Yield</b>	<b>SWIR Detection Limit (kbq/<math>\mu</math>L)</b>
<sup>90</sup> Y	47.3	6.19
<sup>32</sup> P	28.1	10.41
<sup>68</sup> Ga	<b>33.9</b>	<b>8.63</b>
<sup>89</sup> Zr	2.29	127.75
<sup>18</sup> F	1.32	221.63
<sup>131</sup> I	0.669	437.3

**Table 1. The current radioisotope detection limits for SWIR CLI.** The detection limit for the radioisotopes tested in this work are given. Minimum levels are shown based on the detected <sup>68</sup>Ga level of 8.63 kbq/ $\mu$ L and calculated via previously reported relative radiance levels.[3,41]